The Astronomical Journal, 133:612–621, 2007 February

INVESTIGATIONS OF THE MORPHOLOGY OF DUST SHELLS OF COMET C/2001 Q4 (NEAT)

R. Vasundhara
Indian Institute of Astrophysics, Bangalore, India; rvas@iiap.ernet.in

Pavan Chakraborty
Assam University, Silchar, India

S. Muneer
Indian Institute of Astrophysics, Vainu Bappu Observatory, Kavalur, India

G. Masi
Physics Department, University of Rome, Rome, Italy

and

S. Rondi
Laboratoire d'Astrophysique de l'Observatoire Midi-Pyrénées, Université Paul Sabatier, Toulouse III, France
Received 2005 October 21; accepted 2006 September 19

ABSTRACT

The morphology of the dust fans and shells in the images of comet C/2001 Q4 (NEAT) showed significant changes between 2004 April and June due to rapid changes in the Earth viewing and solar illumination geometry. We model the trajectories of dust grains ejected from distributed sources on the comet to explain the observed dust morphology in the images obtained on 2004 April 16, May 12, 16, and 21, and June 3. From the fit to the observations we derive the direction of the rotation pole of the nucleus as $\alpha_p = 270^\circ \pm 10^\circ$ and $\delta_p = 15^\circ \pm 10^\circ$. The derived latitudes of the sources vary between -85° and $+80^\circ$. Six of the sources are found to lie on a single meridian within $\pm 25^\circ$. Using theoretical production rates of water from these sources, reported water production rates, and the archived visual light curve of the comet, we estimate the total active area on the comet to be 38.7 ± 5.8 km^2 near perihelion. The fractional active area on the comet is $12\% \pm 2\%$ or $25\% \pm 4\%$ at perihelion, corresponding to a nuclear radius of 5 or 3.5 km, respectively. The large outgassing areas estimated in the present work can be attributed to the fact that comet 2001Q4 is a comet from the Oort Cloud visiting the inner solar system for the first time.

Key words: comets: general — comets: individual (C/2001 Q4)

Online material: color figures

1. INTRODUCTION

Comet C/2001 Q4 was discovered by the JPL's Near-Earth Asteroid Tracking (NEAT) project on 2001 August 24 using the Palomar 1.2 m Schmidt telescope (Pravdo et al. 2001). Orbit computations by Marsden (2002) indicated that the object was at 10 AU at the time of discovery and that this is its first passage through the inner solar system from the Oort Cloud. Considering its activity at this distance, it was predicted to be a bright comet that would pass through perihelion in 2004 mid-May. For this reason, this comet was the target of detailed spectroscopic studies in visual and IR regions. The comet showed a short dust fan when it was at 8.6 AU from the Sun (Tozzi et al. 2003). Crystalline silicates were discovered in the coma (Wooden et al. 2004) 5 days before perihelion. Wooden et al. also reported changes in the silicate–to–amorphous carbon ratio by a factor of 2 over a period of 2 hr. Images of the comet after application of techniques to remove the smoothly varying cometary background showed complex features with several interwoven sets of shells. The appearance of the complex morphology varied significantly as the Earth viewing and solar illumination geometry changed during the weeks before and after perihelion as the comet's declination changed from -65° in 2004 mid-April to $+45^\circ$ in 2004 early June. Lecacheux & Frappa (2004) derived a rotation period of 23.2 hr for this comet from their time-resolved images. Based on their *Far Ultraviolet Spectroscopic Explorer* observations on 2004 April 24, Feldman et al. (2004) reported a nearly sinusoidal variation of the CO C-X(0,0) band with a period of 17.0 hr.

Knowledge of the pole direction of a comet is important for interpreting nongravitational effects on its orbit during its perihelion passage. Whipple (1978) pointed out that the orientation of the axis of a rotating comet is an important factor influencing the brightness variations. Unlike those of asteroids, rotational light curves of comets can only be obtained at large heliocentric distances before the cometary activity commences. This requires the use of telescopes in the 2 m class or larger. Furthermore, due to restrictions on the observing window, determining the pole direction by inverting the rotational light curve is tedious. Investigations of jets and shells provide a reliable alternative means of estimating the pole direction. These observations are possible for a longer duration of the comet's apparition and provide a large range in heliocentric and Earth viewing geometries. With the availability of CCD receptors in the modern era, detections of even faint jet/shell dust structures in the comae of comets have become possible. These structures have been used to determine the orientation of the axis of rotation of comets such as Hale-Bopp (Sekanina 1998; Vasundhara & Chakraborty 1999), Hyakutake (Schleicher & Woodney 2003), and Wild 2 (Farnham & Schleicher 2005; Vasundhara & Chakraborty 2004). In order to build up a database of the pole orientations of comets of various kinds, we have started a program to model the dust morphology of available comets that show dust features. As part of this program we

TABLE 1
LOG OF OBSERVATIONS OF COMET 2001Q4

Date	UT	Telescope Diameter (cm)	Filter	Image Scale (arcsec pixel^{-1})	T_{exp} (s)	Air Mass	Observing Site
2004 Apr 16.....	23:35	36	O	1.90	1200	2.10	SoTIE (Chile)
2004 May 12.....	14:12	102	*R*	0.38	15	1.26	VBO (India)
2004 May 16.....	21:38	25	O	1.77	120	1.91	Juillan (France)
2004 May 21.....	14:20	102	*R*	0.38	20	1.30	VBO (India)
2004 Jun 3	14:40	102	*R*	0.38	150	1.58	VBO (India)

model the morphology of the dust shells ejected from discrete locations on comet 2001Q4 to derive the orientation of the rotation axis of the nucleus and the location of the active sources. We attempt to obtain an estimate of the fractional area of the derived water-sublimating regions. Extensive brightness measurements have been carried out and documented for this comet starting from its discovery until early 2005 (D. W. E. Green 2005, private communication; observations of comet C/2001 Q4 from the International Comet Quarterly [ICQ] archives). We investigate a possible connection between the variation of the activities of the sources and the visual light curve of the comet.

2. OBSERVATIONS AND DATA PROCESSING

Imaging of comet 2001Q4 was carried out from three stations using the following equipment:

1. Vainu Bappu Observatory (VBO; E78°49′34.8″, N12°34′58″, altitude 725 m). A TK1024 Photometric liquid-nitrogen-cooled CCD was used at the Cassegrain focus (f/13) of the 102 cm telescope on 2004 May 12 and 21 and June 3.

2. Southern Telescopes in Education (SoTIE) at the Las Campanas Observatory (70°42′0″ S29°, altitude 2280 m). The 36 cm Schmidt-Cassegrain telescope on the equatorial mount was used with an Apogee AP-7 CCD camera (512 × 512 pixels, 24 μm × 24 μm each), back-illuminated on 2004 April 16.

3. Juillan, France (N43°21′36″, E0°1′48″, altitude 600 m). A 25 cm Newtonian telescope (f/4) was used along with an Audine camera, Peltier-cooled to −15°C, with a Kodak KAF-401E sensor on 2004 May 16.

Table 1 gives the image scales and the log of these selected observations. Images of a given day, after bias subtraction, flatfielding, and sky subtraction, were stacked after carefully aligning them. The alignment of the images from VBO and Juillan was attempted at subpixel accuracies by determining the comet center in each of the images using the task *imcentroid* of the IRAF package. A centering box of 3 pixels was selected for this task. The task *imshift* of the same package was used to shift the centroids to the middle of the pixel for each image before trimming and stacking. The SoTIE data set was processed using the astronomical image-processing software IRIS. The radial and rotational shift algorithm by Larson & Sekanina (1984, hereafter LS84) was applied to the final images to suppress the strong radial gradient in order to enhance the fainter fan/shell structures. A rotational shift of ±20° around the comet's optocenter was found to be suitable. No attempt was made to apply a radial shift. In the present work we primarily attempt to model the orientation and separation of the dust lanes; hence, this method of delineating the faint features embedded in the coma was found to be adequate. The images on April 16 and May 16 were obtained without filters (O in Table 1) to intercept maximum light. Serious work on dust modeling should be carried out using *R*-band images or narrowband continuum images. The white light images on these dates are contaminated by gaseous emissions. Gas, as well as dust jets, will be enhanced by image-processing techniques. Lara et al. (2001) have delineated CN jet and shell structures in the images of comet Tabur. The possibility of contamination of dust jets/shells by gas jets/shells in our white-light images cannot be ruled out. However, the velocities of expansion of dust and gas being different, the two sets of features should be distinguishable. In our integrated-light images we notice three shells from most of the sources. There has not been any report of a second or third shell of gaseous nature so far. Hence, we start with the assumption that the delineated features in these images are dust related. Furthermore, the April 16 image was needed to increase the time base of the investigations, and the May 16 image fills the gap between the VBO images of May 12 and 21.

3. THE MODEL

The working model that was used to investigate comets Hale-Bopp (Vasundhara 2002; Vasundhara & Chakraborty 1999) and Wild 2 (Vasundhara & Chakraborty 2004) has been used in the present investigation. This model predicts the loci of the dust grains as seen projected on the sky plane relative to the comet at any instant of time. The sources are assumed to emit jets of gas and dust from local sunrise until sunset.

The position of a dust grain with reference to the comet center can be calculated from its initial velocity, the radiation pressure force, and the ejection geometry. On leaving the nucleus radially outward, the dust grains move under the combined force of solar radiation pressure and solar gravity. The gravitational force of the nucleus on the grains is negligible. The initial velocity v_{gr} of the grain is computed using the expression

$$v_{gr} = v\beta^{1/k} \tag{1}$$

(Fulle 1987; Kimura & Liu 1977), where v is a time-dependent constant for the image of a single day and depends on the heliocentric distance at ejection. In the above equation β, the ratio of the force due to solar radiation pressure and the gravitational force on the grain, is given by

$$\beta = F_{rad}/F_{grav} = \frac{3Q_{pr}E_{\odot}}{4\pi cGM_{\odot}}\frac{1}{\rho s}, \tag{2}$$

where Q_{pr} is the scattering efficiency for radiation pressure of the grain and ρ is its density. Here $E_{\odot}$ is the total solar radiation per second, c is the velocity of light, $M_{\odot}$ is the mass of the Sun, and G is the universal gravitational constant. The acceleration on a grain due to solar radiation pressure is $\alpha = \beta g_{sun(1)}/r^2$, where r is the heliocentric distance and $g_{sun(1)}$ is the acceleration due to solar gravity at 1 AU (0.6×10^{-5} km s^{-2}). The value of the parameter k in equation (1) lies between 4 and 6 (Kimura & Liu

TABLE 2
PARAMETERS USED IN THE MODEL

Parameter	Symbol	Value	Status	Ref.
Radius (km)	R_N	3.5	Adopted	An average of the nuclear size on the order of 5–10 km by Tozzi et al. (2003)
Rotation period (hr)	P	23.2 ± 0.25	Adopted	Lecacheux & Frappa (2004)
Hanner (1984) size distribution law parameters	M	7.4	Derived	
	N	3.7	Adopted	Wooden et al. (2004)
	s_0[a]	0.1	Derived	
Grain sizes (μm)	s	0.1–30	Assumed	
Grain refractive index	$\tilde{n}$	1.7−i0.03	Assumed	
Density of grains (g cm^{-3})	ρ	1	Assumed	
Position of rotation axis (J2000.0) (deg)	α_p	270 ± 10	Derived	This work
	δ_p	15 ± 10	Derived	This work
Argument of subsolar point at $T_{\rm Peri}$ (deg)	Φ	219.5	Derived	This work
Obliquity (deg)	I	140.4	Derived	This work

[a] In microns.

1977; Fulle 1987). In the present investigation we use the size distribution law of Hanner (1984), given by

$$n(s)\,ds = (1 - s_0/s)^M (s_0/s)^N. \quad (3)$$

The lower and upper limits on the grain sizes and the constants s_0, M, and N used in the present work are given in Table 2. The last three parameters with $N = 3.7$ were chosen such that the distribution peaks at $s_p = s_0(M + N)/N = 0.3$ μm (Wooden et al. 2004) for this comet. The contribution to the intensity of the dust feature in the R band due to a grain of radius s weighted by the size distribution law (eq. [3]) with the parameters in Table 2 is shown in Figure 1 (*bottom*). It is found that most of the contribution comes from grains in the range 0.2–1.2 μm. The corresponding values of β range between 1.2 and 0.2, as shown in Figure 1 (*middle*). The effect of the grain size on the ejected velocity (eq. [1]) is shown in Figure 1 (*top*). The grain velocities using $k = 4$ and 6 are shown as solid and dashed lines in the top panel, respectively. The width of the shells will be broader with $k = 4$ compared to $k = 6$. The width of the shells is also dependent on the size of the sources, seeing, and, more importantly, on the present technique of delineating the dust features, which is very sensitive to the gradient of the intensity changes. Hence, we make no attempt to derive the parameter k and used the value of 4 following Kimura & Liu (1977).

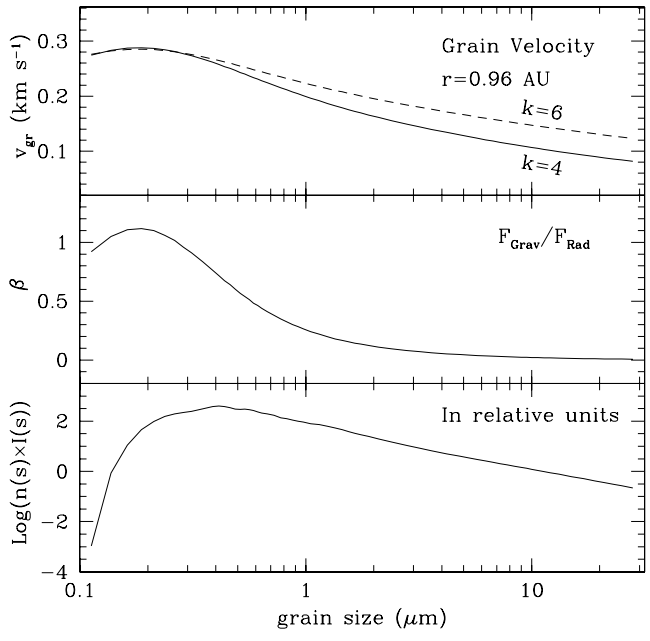

FIG. 1.— Effect of grain size on the ejected velocity β and the total intensity contribution with a grain size distribution with parameters in Table 2.

4. FIT TO THE DATA

4.1. *Pole Orientation and Source Locations*

The simulations were carried out to include grains ejected during three to four rotations. To understand the morphology of the dust features, assumptions of spherical grains and Mie scattering were considered adequate to compute the light-scattering functions and $Q_{\rm pr}$ in equation (2). The dust morphology as seen from the Earth depends on (1) the right ascension and declination of the northern rotation pole of the nucleus, (2) the latitude of the sources on the nucleus, and (3) the rotation period of the nucleus. The separation of the shells of successive rotations depends on the distance traveled by the grains in the interval between two rotations. This distance can be fitted by adjusting the grain velocities, provided the rotation period is known precisely. In the present work we assumed the rotation period to be 23.2 hr (Lecacheux & Frappa 2004). The parameter v in equation (1) was adjusted to match the separation of the shells. This parameter will change if the rotation period is revised. Complex dust morphology in the processed images implies multiple jets. For an unbiased search of the pole direction, we consider sources evenly distributed on both sides of the cometary equator at $\pm 80^\circ$, $\pm 60^\circ$, $\pm 30^\circ$, and 0° latitudes. For a zero-order fit we tried all combinations of (α_p, δ_p) in the range $0^\circ \le \alpha_p \le 360^\circ$ and $-90^\circ \le \delta_p \le +90^\circ$ at increments of 20° for the five dates. Each orientation (α_p, δ_p) is associated with unique values of P, the position angle of the projection of the north pole of the nucleus on the sky plane, and B and B', the cometocentric latitudes of the sub-Earth and sub-Sun points. For the diametrically opposite orientation $(\alpha_p - \pi, -\delta)$ P becomes $P + 180$ and B and B' become $-B$ and $-B'$, respectively. With the assumption of a set of sources symmetric with respect to the comet's equator, the jet/shell structures will appear similar in the two cases except for changes in the direction of winding of the shells. Sample simulations are shown in Figures 2 and 3 for April 16 and May 16 for $\alpha_p = 100^\circ$–320°, restricted to only the relevant range in α_p that matches the observations for better clarity.

The pole orientations that produce morphology resembling the observations are marked with a black circle at the upper right

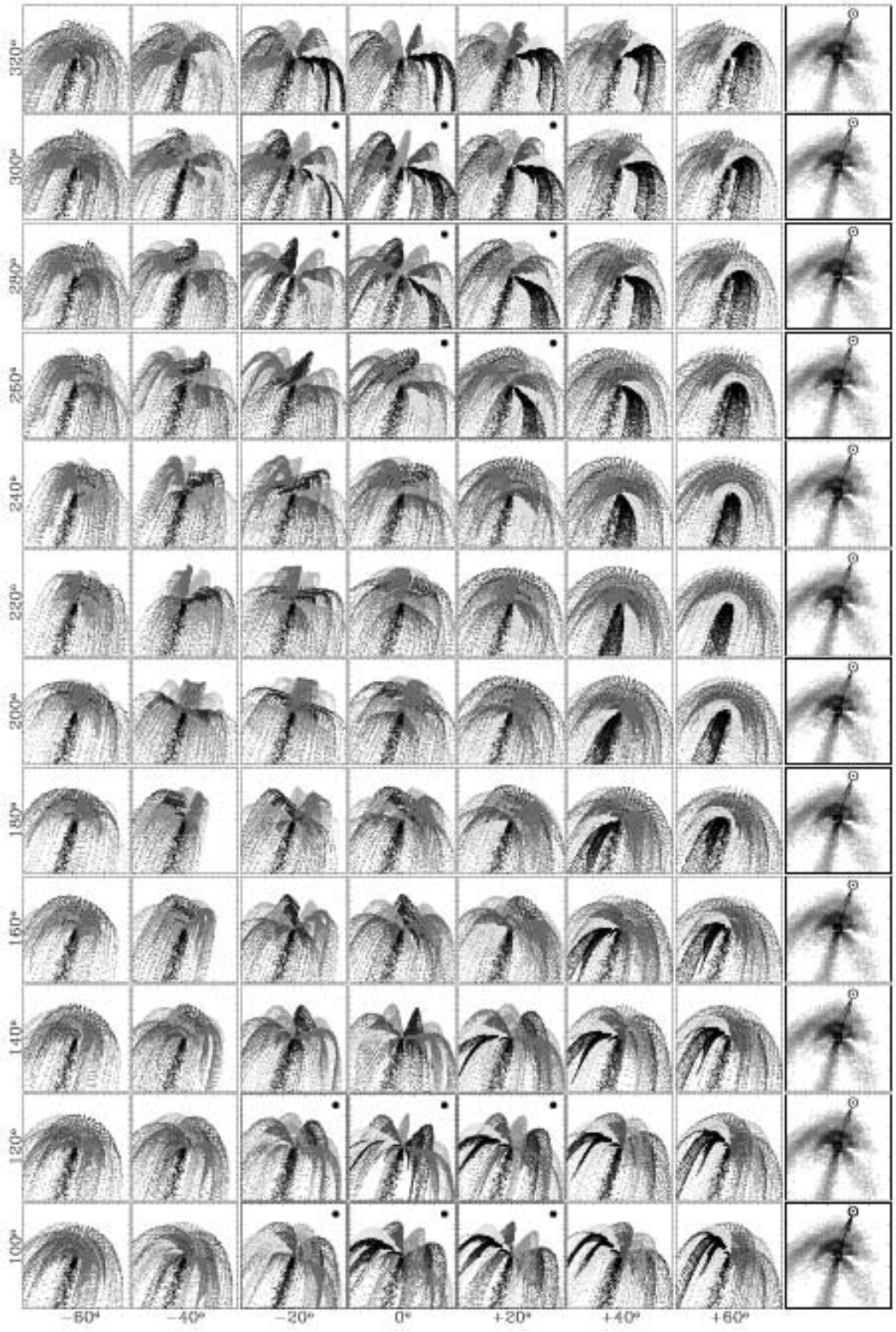

FIG. 2.— Variation of jet morphology with pole orientation on 2004 April 16. Latitudes and color codes are given in Table 4. [*See the electronic edition of the Journal for a color version of this figure*.]

corner in Figures 2 and 3. Further fitting was carried out by superposing the simulations on the images. The pole coordinates and the latitude of the sources were adjusted at smaller grid intervals of 10° to match the orientation of the sets of shells on all the dates. The distance of the shells from the nucleus depends on the hour angle of the Earth $HA_{\oplus}$ as seen by the source. The adjustments of the two parameters v and $HA_{\oplus}$ were carried out iteratively until the shell positions and separations matched. The fits indicated two possibilities: case A: $\alpha = 270^{\circ}$, $\delta = +15^{\circ}$, with sources at +80°, +45°, +18°, −2°, −35°, −60°, and −85°; and case B: $\alpha = 90^{\circ}$, $\delta = -15^{\circ}$, with sources at −80°, −45°, −18°, +2°, +35°, +60°, and +85°. We make use of the *R*-band image of

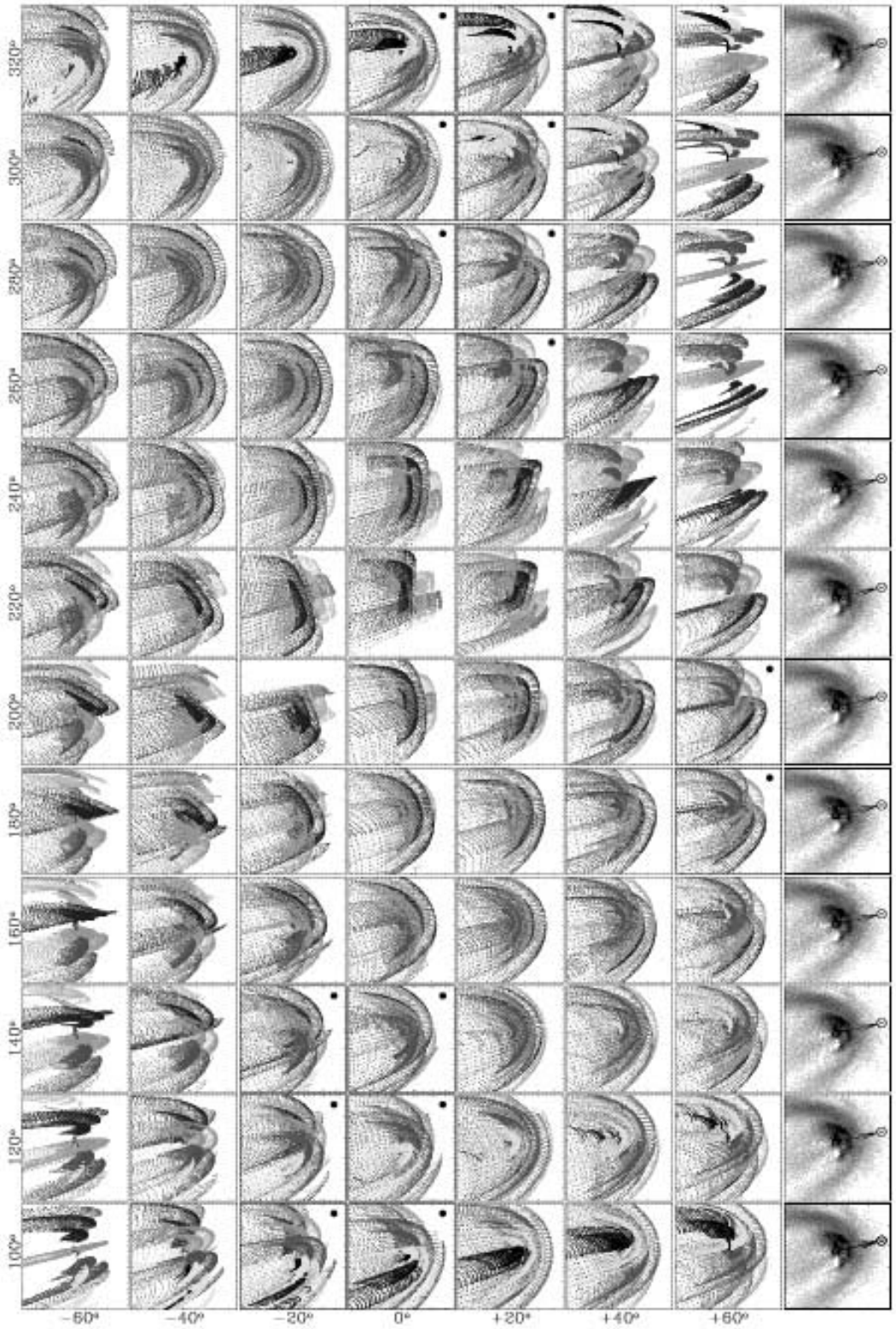

FIG. 3.— Variation of jet morphology with pole orientation on 2004 May 16. Latitudes and color codes are given in Table 4. [*See the electronic edition of the Journal for a color version of this figure*.]

May 12 to investigate the inner spiraling regions and the next outer envelope of the previous rotation to select between the two possibilities (Fig. 4). The pole orientation $\alpha = 270^\circ$, $\delta = +15^\circ$ (*top right*) produces counterclockwise rotating jets resembling the observed features. The inner jets point in the same direction as in the observed image. The same direction has been noted by Lecacheux & Frappa (2004). The pole orientation $\alpha = 90^\circ$, $\delta = -15^\circ$ (*bottom right*) produces inner jets unwinding in the opposite direction. Further checks are made by comparing the distances of the morning and evening sectors of the next envelope from the nucleus. The morning sector corresponding to ejection at sunrise should be farther away compared to the evening sector ejected later at sunset.

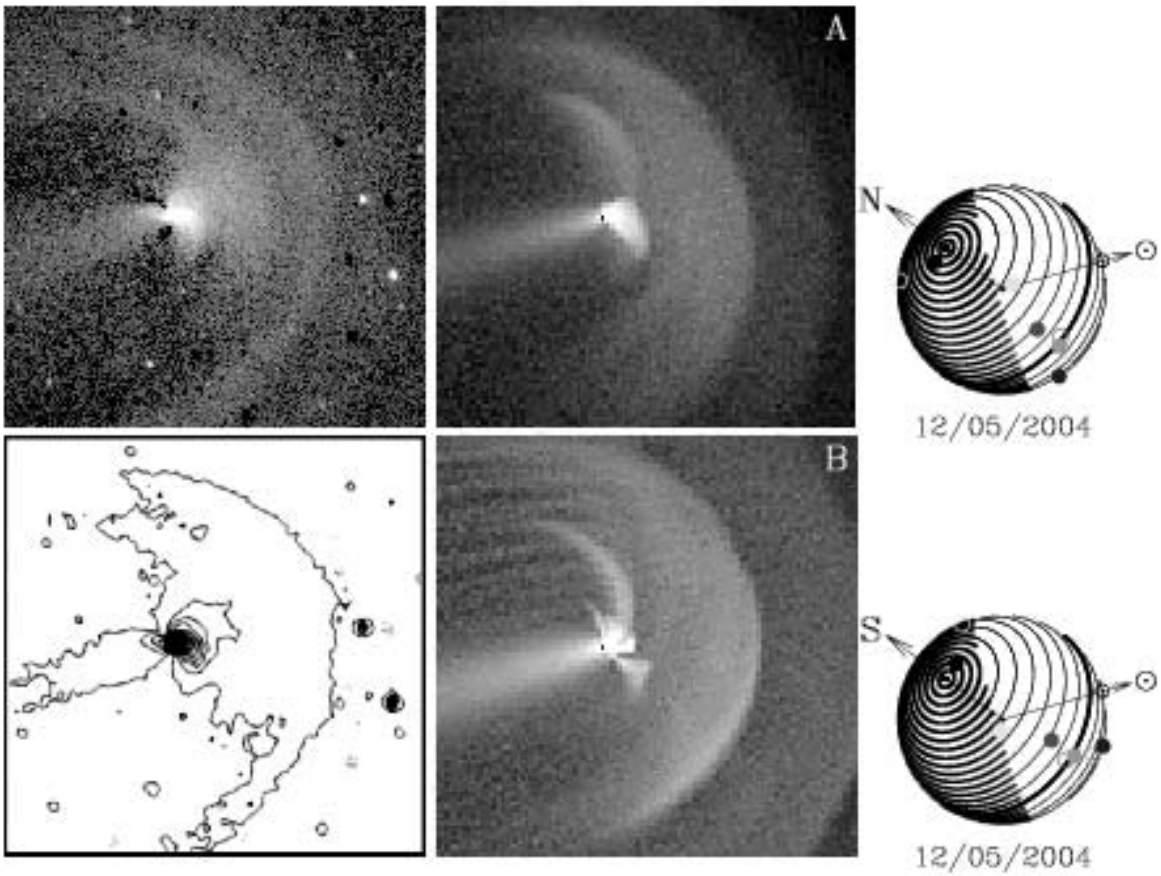

FIG. 4.—Effect of the sense of rotation of the nucleus on the jet/shell morphology. *Top left*: Observed image of 2004 May 12, after LS84 filtering. *Bottom left*: Contour map of the top left image. *Top right*: Case A, a simulated image of dust features for the nuclear pole orientation $\alpha = 270^\circ$, $\delta = +15^\circ$. *Bottom right*: Case B, the same, but for orientation $\alpha = 90^\circ$, $\delta = -15^\circ$. Case A is the preferred choice because (1) it produces counterclockwise rotating inner jets resembling the observed features and (2) the location of the northern end of the next observed envelope matches with the location of the evening branch of the simulation of case A. The evening sector corresponding to ejection at sunset is closer compared to the morning sector ejected earlier at sunrise. For case B this end of the envelope was ejected at sunrise and hence is too far away. Corresponding nuclear orientation and relative source locations are shown to the right of each panel. [*See the electronic edition of the Journal for a color version of this figure.*]

The location of the northern sector of the observed envelope matches with the location of the evening sector of the simulation of case A. For case B this end of the envelope is ejected at sunrise and hence is too far away. We therefore select pole solution A. The uncertainty of $\pm 10^\circ$ in the derived pole position (Table 2) includes the uncertainty in fitting individual images by visual superposition and also the spread in the fits to the five images. The uncertainty in the latitude of the sources arises partly from the uncertainty in the pole solutions. The cometocentric latitude of the Earth (B) and the Sun (B') and the position angle of the projected north pole of the nucleus (P) for the fitted pole direction are given in Table 3. The cometocentric longitude U' of the sub-Sun point measured from the node of the comet's equator on the ecliptic along the direction of rotation of the comet is also given.

The simulated images on the five dates of observation are shown in the second column of Figure 5. These images were generated taking into account the location and scattering efficiency of the grains with the size distribution parameters given in Table 2. The images in the first column are the observed images after processing using the LS84 filter. In order to illustrate the orientation and shape of the shells/jets from the sources at different latitudes, the locations of the dust grains are overplotted on the contour map of the observed images in the third column, with color codes for the source latitudes given in Table 4. The

TABLE 3
VIEWING AND ILLUMINATION GEOMETRY OF COMET 2001Q4

DATE	α_C (J2000.0)	δ_C (J2000.0)	Δ (AU)	r (AU)	U' (deg)	P (deg)	B (deg)	B' (deg)	ΔT[a] (days)	GRAIN VELOCITY (km s^{-1}) 0.2 μm	2.0 μm
2004 Apr 1	02 54 46.1	−65 12 22	0.6999	1.0856	231	235	31	0	−28.99	0.30	0.17
2004 May 1	08 16 05.7	+09 48 36	0.3713	0.9638	203	54	48	−21	−3.36	0.38	0.22
2004 May 1	08 43 00.3	+23 45 24	0.4556	0.9621	198	50	34	−25	0.93	0.38	0.22
2004 May 2	09 05 09.8	+33 26 26	0.5691	0.9670	191	50	25	−28	5.63	0.38	0.22
2004 Jun 3	09 44 12.2	+46 17 38	0.9146	1.0155	171	55	11	−36	18.65	0.36	0.20

NOTE.—Units of right ascension are hours, minutes, and seconds, and units of declination are degrees, arcminutes, and arcseconds.
[a] Days since perihelion.

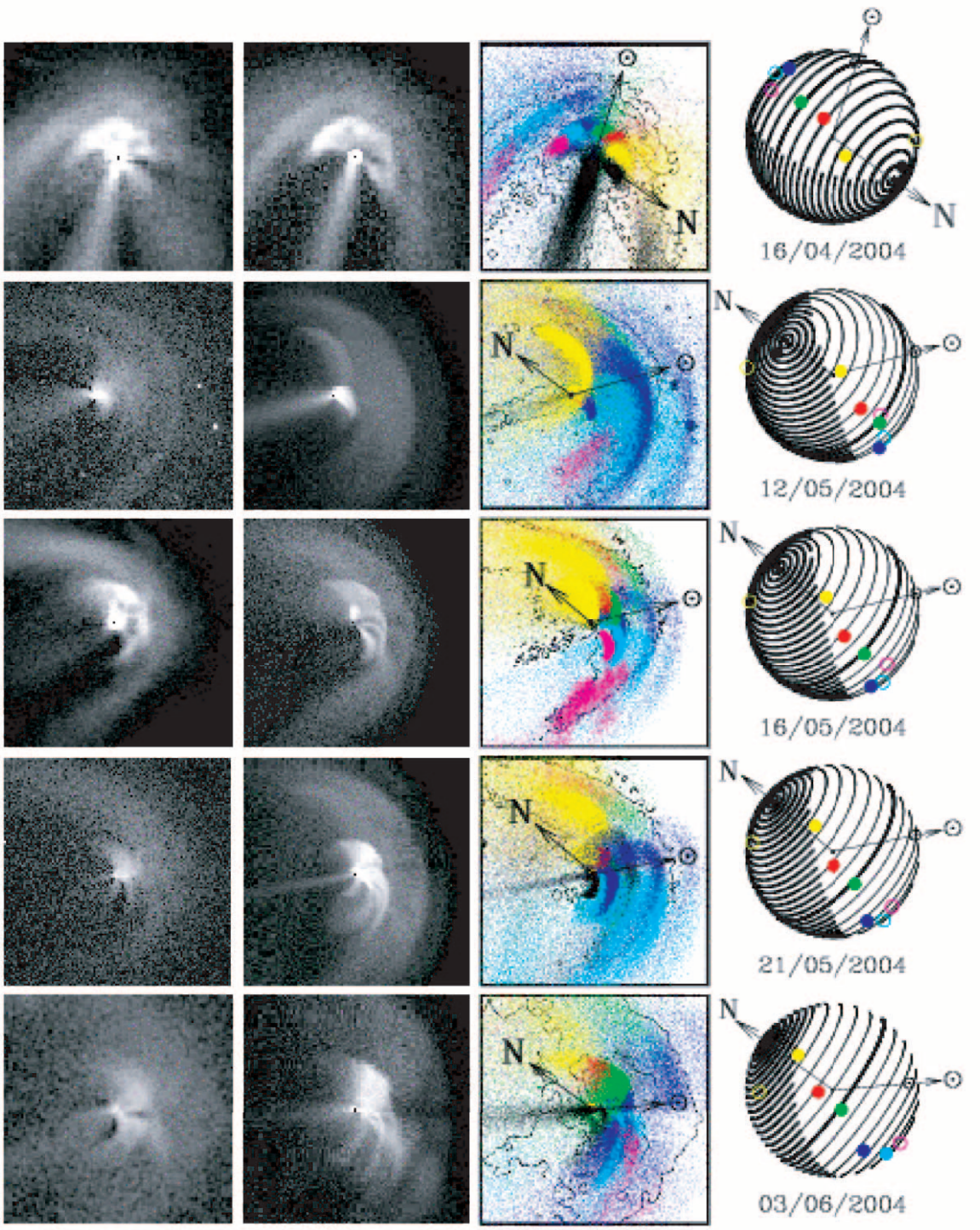

FIG. 5.—*First column*: Observed images after processing using the LS84 filter. *Second column*: Simulated intensity maps. *Third column*: Locus of dust grains ejected from different sources plotted on the contour map of the observed images (the color codes are listed in Table 4). Image scales are 7.3 (2004 April 16), 5.2 (2004 May 12), 14.6 (2004 May 16), 4.9 (2004 May 21), and 3.9 (2004 June 3) in units of 10^4 km on a side (144″, 192″, 248″, 154″, and 77″, respectively). *Fourth column*: Orientation of the nucleus, assumed to be spherical in the model. Relative longitudes and latitudes of the illuminated sources are shown with the same color code. The night side of the nucleus is shown shaded.

projected directions of the northern rotation pole of the nucleus on the date are shown. The fourth column of Figure 5 shows the derived orientation of the nucleus, assumed to be spherical in the model. The shaded regions on the nucleus are unilluminated regions. The relative locations of the illuminated sources are plotted with the same color code as the jets. Filled circles indicate sources facing the Earth, and open ones are on the far side but illuminated. Prominent dust tails in the anti-Sunward direction are noted in the images of April 16 and May 12 and 21. For a realistic match with the observations, simulation of the dust tail is included for these dates. The dust tail is color-coded black.

The "knotted" structures in the April 16 images could only be reproduced by restricting the activity of the sources at +45°, +18°, and −2° to ±20° of local noon. It is not known whether

TABLE 4
Source Latitudes, Color Codes, and Derived Areas

Latitude (deg)		Grain Size		Area (km^2)				
Figs. 2 and 3	Fig. 5 (±10°)	(μm)	Color in Fig. 5	60 days BP[a]	10 days BP	P[b]	10 days AP[c]	60 days AP
−80	−85	0.1–30	Magenta	PN[d]	2.2	2.2	2.2	2.2
−60	−60	0.1–30	Cyan	2.5	2.5	2.5	2.5	2.5
−30	−35	0.1–30	Blue	5.7	5.7	5.7	5.7	5.7
0	−2	0.1–30	Green	4.7	4.7	4.7	4.7	4.7
+30	+18	0.1–30	Red	3.1	3.1	3.1	3.1	3.1
+60	+35[a]	0.1–30	Yellow	NA[e]	7.9	7.9	7.9	7.9
	+45	0.1–30	Yellow	12.6	12.6	12.6	12.6	12.6
+80	+80	0.1–30	Black	28.3	PN	PN	PN	PN
	−30[f]	0.05	Black	NA	NA	NA	0.6	3.4
	−60[f]	0.05	Black	NA	NA	NA	0.6	3.4
Total area (±5.8)				56.9	38.7	38.7	39.9	45.5

[a] BP, before perihelion.
[b] P, at perihelion.
[c] AP, after perihelion.
[d] PN, polar night.
[e] NA, not active.
[f] Active after May 21.

this is an artifact of the image processing or a real effect of local topology. The north polar source at +80° is active only in the April image, while the source at +35° does not appear to have commenced its activity at this epoch. The shells due to sources at +45°, +18°, and −2° are well resolved in this image. The drastic change in appearance of the May 12 and 16 images separated by 103.43 hr or 4.458 rotations does not come as a surprise. These two images represent shell structures 165° apart in phase. On the former date the shells are very close to the nucleus and just unfolding. In the latter case the shells are farther away. The spokes in the white-light image of May 16 could not be reproduced from the dust modeling. It is possible that these are of gaseous nature.

The fits have been carried out assuming a period of 23.2 hr (Lecacheux & Frappa 2004). The derived value of v in equation (1) depends on the rotation period. The grain velocities given in Table 3 are derived from the fitted value of v. These values are revised by a factor $23.2/T_{\rm New}$ to a first-order approximation when the period is revised to $T_{\rm New}$. However, the rotation period cannot be drastically different from the present value because the shapes of the shells change with the period of rotation due to the cumulative effect of the solar radiation pressure forces during one rotation period. In the case of a slowly rotating nucleus, there would be more asymmetry on the dawn and dusk sides (Sekanina & Larson 1984). Furthermore, successive shells would be depleted of smaller grains of high β much faster than the shells of a quickly rotating nucleus. We decreased the rotation period by up to 20% and increased v by 20% for the trial fits in Figure 3. The direction of the pole and the overall pattern of the jet/shell structures did not change significantly. However, differences in the cumulative effects of radiation pressure forces began to be noticeable. The effects would be the same if one changed the grain size distribution. Simulations of shorter period have less sweeping of the grains in the anti-Sunward direction; this effect would be the same if the grains were larger and experienced less radiation pressure. Thus, the success of the fit in getting information on the grain size distribution and grain types depends on precise knowledge of the rotation period. The derived pole solutions and source latitudes are, however, robust, because these depend on the overall morphology. A larger number of sources for this comet has aided in better constraining the pole solution.

4.2. *Relative Longitude of the Active Sources*

The uncertainties in the rotation period are compensated for by adjusting the grain velocity parameter v in equation (1). However, to determine the longitude of the sources in reference to a fixed meridian on the comet, it is important to know the precise rotation period. Furthermore, the rotation period determined from observations is not exactly the sidereal period but a synodic one (Sekanina 1991). Hence, care is needed when comparing the derived longitudes of the sources in images taken several days apart. Due to a lack of data at close intervals of time, no attempt has been made to determine the absolute longitude of the sources. The relative longitudes of the sources are equal to the separation of the derived hour angles of the Earth ($HA_{\oplus}$; § 4.1) as seen from the sources at any instant. These are found to be better constrained on the five dates of our observations. Figure 6 shows the derived relative longitudes of the sources versus their latitudes on the five

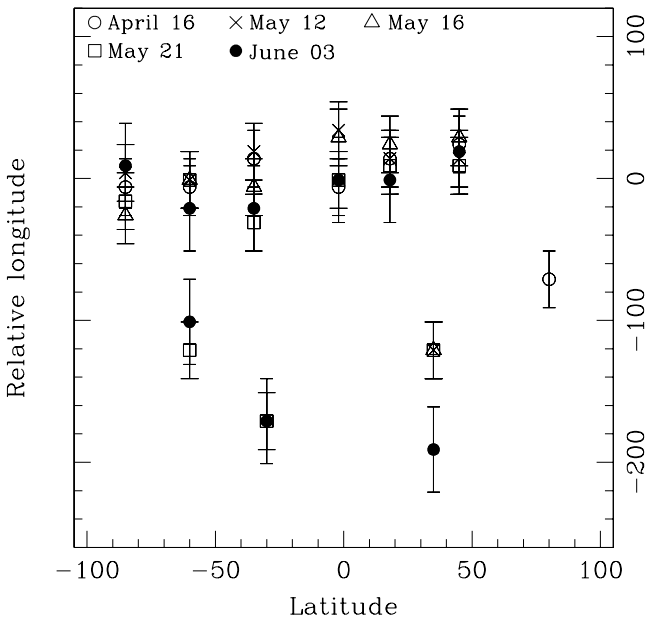

Fig. 6.—Latitude and relative longitude of the active sources on comet 2001Q4.

dates. Six of the sources appear to be located on a meridian within $\pm 25^\circ$.

All the sources that were found to be active from April to June are on this belt, except for the source at latitude $+35^\circ$. The near–north polar source at $+80^\circ$ was sunlit only in April. The southward sharp features in the May 21 and June 3 images could be explained by invoking additional sources at -30° and -60°. These features appear narrow and are seen close to the nucleus. The shape of these features suggests the presence of dust grains of sizes such that these are lifted with velocities approaching the gas velocity with negligible radiation pressure force acting on them. Such dynamics can be attributed to grains smaller than 0.05 μm. Another possible explanation could be that these are in reality gas jets with emission bands in the wing of the *R*-band observations during May 21 and June 3.

5. CONSTRAINING THE AREA OF THE SOURCES

5.1. *Relation between Visual Magnitude and Water Production Rate*

The technique of delineating fine structures using the LS84 algorithm does not conserve the original flux. The gradients of the features influence the sharpness and intensity of the resolved features. In order to assess the area of the individual sources, we compute the sublimation rate Z of water (in molecules cm^{-2} s^{-1}) from the 10 sources following the method of Sekanina (1988) for the period ± 200 days from the date of perihelion passage of the comet. This method yields the rotation-averaged water sublimation rate per unit outgassing area and implicitly takes into account the duration of activity of a source per rotation cycle depending on its latitude and the latitude of the sub-Sun point. The total computed water production rate from all the active regions is

$$Q^C_{\mathrm{H_2O}} = \sum_{n=1}^{10} Z(n)\mathrm{area}(n). \quad (4)$$

To determine the area of the sources in the above equation, we make use of the relationship between the visual magnitude normalized at 1 AU from the Earth and the water production rate suggested by Festou (1986) of the form

$$\log (Q_{\mathrm{H_2O}}) = A - Bm_v. \quad (5)$$

Festou (1986) obtained $A = 32.04$ and $B = 0.4$ based on 28 observations of 16 comets for the OH production rate. Jorda et al. (1992), from the study of 13 comets, arrive at $A = 30.74 \pm 0.02$ and $B = 0.24 \pm 0.003$ for the water production rate. In the present study the observed visual magnitudes were obtained from the ICQ archives (D. W. E. Green 2005, private communication). Data points by 24 observers that were mutually consistent were selected. The observed magnitudes were normalized to 1 AU from the Earth using the relation

$$m_v = m_v(\mathrm{obs}) - 5 \log (\Delta). \quad (6)$$

Water production rates of $\log (Q_{\mathrm{H_2O}}) = 29.01 \pm 0.02$, 29.10 ± 0.02, 28.95 ± 0.02, and 28.90 ± 0.02 on 2004 May 11 and 12 and June 9 and 10, respectively, by D. G. Schleicher (2006, private communication) were used in the study. Due to the proximity of the two dates of observations in May and June, the mean data of each month were used. The water production rates and the interpolated values of visual magnitudes 5.39 ± 0.22 and 6.15 ± 0.19 from the ICQ data set on these dates were used to derive the values of $A = 30.38 \pm 0.05$ and $B = 0.237 \pm 0.029$.

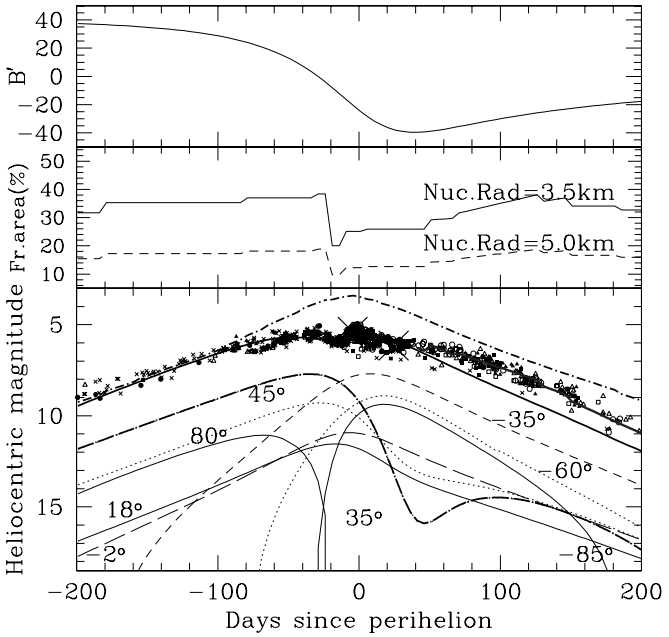

FIG. 7.—*Top*: Variation of the cometocentric latitude of the Sun with time computed using the fitted pole positions. *Bottom*: Various symbols (one for each of four observers) indicating the observed magnitudes compiled from the ICQ archives (D. W. E. Green 2005, private communication) and normalized to 1 AU Earth distance. The solid fitted line represents the total contribution from the latitude and areas of the sources given in Table 4 computed using eq. (7). The thick solid line represents the synthetic light curve obtained by including additional activity 40 days after perihelion to fit this part of the observed data. The activity of the individual sources is shown with shifts in magnitude for better clarity. The dot-dashed line represents the synthetic light curve of the comet of uniform activity during the entire apparition.

This value of B is close to the results of Jorda et al. (1992). The derived uncertainty in these coefficients arises from the uncertainty in the interpolated value of the visual magnitude due to scatter in the light curve and the uncertainty of the water production rate quoted by D. G. Schleicher (2006, private communication).

5.2. *Fit of the Observed Light Curve with the Simulated Light Curve: Estimation of Water Sublimation Area*

The visual magnitudes normalized to the Earth distance of 1 AU are shown in Figure 7. The data points have been plotted with six different symbols to represent observations by 24 observers. Each symbol type represents data by four observers. This helps in understanding the cause of scatter, which can arise due to (1) observational uncertainty in individual measurements or (2) differences in observing methodology and telescope aperture. The effects of the former are random, while the latter are found to show certain trends. The coefficients A and B in § 5.1 were derived using the data points shown as large crosses on the light curve. The dot-dashed line is the synthetic light curve of the comet of uniform activity during the entire apparition. The curve was constructed using the derived values of A and B. The area of the water sublimation region was adjusted to match this curve to the preperihelion branch of the observations, because in this region the slope matches. Figure 7 shows that the brightness of the comet started deviating from this prediction about 80 days before perihelion and never recovered. This indicates the need for considering additional factors such as the seasonal effects on the activity of the sources. We investigate this possibility by summing the contribution from the derived sources during the ± 200 days of the perihelion passage. The individual synthetic light curves of the sources were generated by converting $Q^C_{\mathrm{H_2O}}$ (computed

using eq. [4]) to visual magnitude m_Q using the derived values of A and B in the relation

$$m_Q(n) = A/B - \log\left[Q^C_{H_2O}(n)\right]/B. \quad (7)$$

The $m_Q(n)$ values of eight of the sources (Table 4) are shown with magnitude shifts for better clarity. The activity of a source is governed by its latitude and the cometocentric latitude (B') of the Sun. As shown in Figure 7 (*top*), the value of B' changed very gradually from a value of 40° to around 30° from discovery until mid-February. The Sun remained circumpolar for latitudes northward of 55°. The preperihelion activity is therefore dominated by the northern sources at 80° and 45°. The fall in activity of the 80° source, sharp changes in the production rate of the 45° source, and the activation of the −85° source due to rapid changes in B' appear to be responsible for the flat, asymmetric, double-humped shape of the light curve near perihelion. The location of the abrupt increase in brightness by about 0.5 mag in the light curve around 10 days before perihelion, consistently measured by several observers, may be due to the onset of activity of the 35° source.

The areas of the individual sources were adjusted to match the shape and the magnitude level of the observed light curve. The total fractional areas active on different dates are shown in Figure 7 (*middle*). The fitted theoretical light curve is shown as the solid line in the bottom panel. The fit was carried out by a visual comparison of the curve to the data points. The synthetic light curve matches the observations up to about 40 days after perihelion. Thereafter, the observed magnitude appears to fall more slowly than predicted by the slope parameter $A = 0.237$. The activity appears to be more sustained despite increasing heliocentric distance. The reason for the enhanced activity could be an increase in active area. Local topology favoring higher light gathering at these times compared to perihelion days is another possibility, because the values U' and B' of the sub-Sun point change continuously (Table 3). We attempted to increase the area of the active regions to match this part of the light curve. The regions likely to get hyperactivated will be those in the southern regions because B' is negative. Hence, we increased the areas of the new sources at −30° and −60°. An increase in the activity of the older sources at −35° and −60° or some fresh activity in this region will have the same effect. The total active area that is needed to explain this part of the light curve is as shown in the middle panel of Figure 7, while the thick solid line in the bottom panel represents the synthetic light curve.

The fitted areas of the sources in square kilometers are given in Table 4. The areas of the sources, especially the three northern sources, are strikingly large. The source at +80°, being large, must be covering almost the entire north polar region. The areas of the two active regions on the periodic comet Enke 1 have been estimated by Sekanina (1988) to be as small as 0.4 and 0.6 km^2. The areas of the two active regions on comet Wild 2 were estimated at 4.5 and 9.5 km^2 by Sekanina (2003), and the author therein notes that the comet's short history in the innermost solar system could account for the large outgassing areas. The large outgassing areas estimated in the present work can be attributed to the fact that comet 2001Q4 is a new comet visiting the inner solar system for the first time.

6. CONCLUSION

The dust morphology around comet C/2001 Q4 (NEAT) changed during our observations from 2004 April 16 to June 3 due to rapid changes in the Earth-comet-Sun geometry. The images were fitted using our photodynamic model to derive the direction of the rotation axis of the nucleus as R.A. = 270° ± 10° and decl. = +15° ± 10°. The latitudes of the sources were determined by fitting the orientation of the sets of shells. Analysis of the interwoven sets of shells indicates the presence of eight sources with latitudes between −85° and +80° on the comet until perihelion. Two more sources are needed to explain the postperihelion images. The locations of six of the sources appear to fall on the same meridian within ±25°. We attempt to constrain the size of the sources on the comet responsible for water production. The derived total active area of sublimation of water at perihelion of 38.7 ± 5.8 km^2 is significantly large. The reason for this extensive activity could be that this comet is from the Oort Cloud and entering the inner solar system for the first time (Marsden 2002). This argument is further strengthened by the fact that this comet showed the presence of activity when it was as far as 8.6 AU (Tozzi et al. 2003). A nuclear radius of size larger than 5 km is another possibility.

We are grateful to Professor Z. Sekanina for several useful discussions. We thank D. G. Schleicher for permitting us to use his production rate measurements of comet 2001Q4. We wish to thank F. Mallia for his help in the observations from SoTIE. One of us (G. M.) wishes to thank the Telescope In Education (TIE) team for their collaboration and for allowing us to use their SoTIE telescope. Another of the authors (P. C.) is thankful to IUCAA for sponsoring his research under the IUCAA visiting associateship program. The observations were part of an education project managed by G. Masi and F. Mallia. We thank A. Rondi for his valuable participation in the observations from Juillan, France.

REFERENCES

Farnham, T. L., & Schleicher, D. G. 2005, Icarus, 173, 533
Feldman, P. D., et al. 2004, BAAS, 36, 1121
Festou, M. C. 1986, in Asteroids, Comets, Meteors II, ed. C.-I. Lagerkvist (Uppsala: Uppsala Univ.), 299
Fulle, M. 1987, A&A, 171, 327
Hanner, M. S. 1984, Adv. Space Res., 4, 189
Jorda, L., Crovisier, J., & Green, D. W. E. 1992, in Asteroids, Comets, Meteors 1991, ed. A. W. Harris & E. Bowell (Houston: LPI), 285
Kimura, H., & Liu, C. P. 1977, Chinese Astron., 1, 235
Lara, L. M., Schulz, R., Stüwe, J. A., & Tozzi, G. P. 2001, Icarus, 150, 124
Larson, S. M., & Sekanina, Z. 1984, AJ, 89, 571 (LS84)
Lecacheux, J., & Frappa, E. 2004, IAU Circ. 8349
Marsden, B. 2002, Minor Planet Circ. 46619
Pravdo, S. H., Helin, E. F., & Lawrence, K. J. 2001, IAU Circ. 7695
Schleicher, D. G., & Woodney, L. M. 2003, Icarus, 162, 190
Sekanina, Z. 1988, AJ, 95, 911
———. 1991, AJ, 102, 350
———. 1998, ApJ, 494, L121
———. 2003, J. Geophys. Res., 108, 8112
Sekanina, Z., & Larson, S. M. 1984, AJ, 89, 1408
Tozzi, G. P., Boehnhardt, H., & Lo Curto, G. 2003, A&A, 398, L41
Vasundhara, R. 2002, A&A, 382, 342
Vasundhara, R., & Chakraborty, P. 1999, Icarus, 140, 221
———. 2004, ApJ, 616, 1278
Whipple, F. L. 1978, Moon Planets, 18, 343
Wooden, D. H., Woodward, C. E., & Harker, D. E. 2004, ApJ, 612, L77